Noninvasive optical monitoring of pulmonary embolism: a Monte Carlo study on visible Chinese human thoracic tissues

Shuo Meng,[a,b] Hengjie Su,[a] Jianghui Guo,[a,c] Lingxiao Wang,[a] and Ting Li[a,d,*]

[a]Chinese Academy of Medical Sciences, Institute of Biomedical Engineering, Peking Union Medical College, Tianjin, China
[b]Tiangong University, Tianjin, China
[c]University of Electronic Science and Technology of China, Chengdu, China
[d]Chinese Institute for Brain Research, Beijing, China

Abstract

Significance: In recent years, the incidence rate of pulmonary embolism (PE) has increased dramatically. Currently, the correct diagnosis rate of PE in China is relatively low, and the diagnosis error rate and missed diagnosis rate were as high as about 80%. The most standard method of PE detection is pulmonary artery digital subtraction angiography (DSA), but pulmonary artery DSA is an invasive examination, and patients can have certain risks and discomfort. Noninvasive monitoring of PE remains challenging in cardiovascular medicine.

Aim: We attempt to study the light propagation in human thoracic tissues and explore the possibility of near-infrared spectroscopy (NIRS) in noninvasive detection of PE.

Approach: In this study, by utilizing the Monte Carlo simulation method for voxelized media and the Visible Chinese Human dataset, we quantified and visualized the photon migration in human thoracic region. The influence of the development (three levels) of PE on the light migration was observed.

Results: Results showed that around 4.6% light fluence was absorbed by the pulmonary tissue. The maximum signal sensitivity distribution reached 0.073% at the 2.8- to 3.1-cm light source–detector separation. The normalized light intensity was significantly different among different PE levels and formed a linear relationship ($r^2 = 0.998$, $p < 10^{-5}$).

Conclusions: The study found that photons could reach the pulmonary artery tissue, the light intensity was linearly related to the degrees of embolism, PE could be quantitatively diagnosed by NIRS. Meanwhile, the optimized distance in between the light source and detector, 2.8 to 3.1 cm, was recommended to be used in future potential noninvasive optical diagnosis of PE.

 [DOI: 10.1117/1.JBO.28.1.015001]

Keywords: pulmonary embolism; near-infrared spectroscopy; Monte Carlo simulation; light fluence; signal sensitivity distribution.

Paper 220142GRR received Jun. 28, 2022; accepted for publication Dec. 13, 2022; published online Jan. 18, 2023.

1 Introduction

Pulmonary embolism (PE) refers to a clinical and pathophysiological syndrome that commonly occurs as a cardiovascular disease.[1] It shows pulmonary circulation disorders and even pulmonary infarction that are caused by endogenous or exogenous emboli block of the pulmonary artery or its branches. According to a report,[2] the incidence of PE was the second only to coronary heart disease and hypertension in cardiovascular diseases, which is equivalent to 1/2 of the

*Address all correspondence to Ting Li, t.li619@foxmail.com

incidence of acute myocardial infarction; the mortality rate ranks third, the clinically observed acute PE mortality rate is not lower than that of myocardial infarction.[3] The most accurate PE detection method is the pulmonary artery digital subtraction angiography (DSA), which is the gold standard for the PE diagnosis with almost 100% accuracy. However, this examination method is invasive and easy to cause damage to blood vessels or surrounding tissues. Besides, complications frequently occur after examination that also limit the DSA application.[4] Another frequently used clinical noninvasive detection is the computer tomography pulmonary angiography (CTPA), which can detect pulmonary artery emboli through morphological character analysis, thus providing a basis for the PE diagnosis. However, due to the complex vascular structure below the pulmonary artery subsegment and the large interference outside the slice, the diagnostic efficiency of this part of embolus is reduced. Therefore, noninvasive detection of PE remains a challenge in cardiovascular medicine.

Near-infrared spectroscopy (NIRS) is based on the spectral characteristics of oxygenated hemoglobin (HbO2) and deoxygenated hemoglobin (HbO)[5] and quantitative determination of tissue hemoglobin oxygen saturation for measure disease. Since its invention in the 1970s, with its advantages of noncontact, noninvasive, and online rapid detection, it has been used in a series of clinical human body studies with validated results.[6] In recent years, great progresses in NIRS research were on human brain,[7,8] heart,[9] lung,[10,11] and mammary gland.[12] Accurate tissue modeling of tissue increases the utility of photon migration for a broader range of applications. NIRS can detect up to a few centimeters that are enough to penetrate the thorax and reach the pulmonary artery.[13] However, the study of photon migration in human pulmonary artery region has not been thoroughly studied, and noninvasive optical technology has great prospects in clinical PE detection.

In previous studies, hemodynamic abnormalities occurred first with PE, followed by characteristic events associated with hypoxemia. It was evident that the right ventricular blood reperfusion into the pulmonary artery was in disorder under the instance of pulmonary artery lesions (e.g., increased levels of embolism). The changes of hemodynamic provided physiological basis for direct detection of PE under hypoxemia.[14] At present, the migration rules of NIR light in the pulmonary artery are not clear, so it is impossible to determine where to place the light source and detector (LSD) and how much the separation of the LSD can better detect the signal sensitivity distribution (SSD). This is also an urgent problem to be solved to achieve the clinical application of noninvasive PE detection.

It is very important to obtain the quantitative characteristics of photon migration in the thoracic tissues model under noninvasive detection mode and to study the optimal design of light source detector placement. This study aimed to solve these problems. Before to know whether PE could be detected by the optical method, the photon transmission rules in pulmonary tissues were needed to understand. The photon transmission of human body was complicated. To be more clarified, the pulmonary artery study was simulated on a three-dimensional (3D) structure, VCH is the best choice. The VCH is an individualized 3D heterostructure model,[15] which is suitable for the simulation of 3D voxel media. The VCH has played an important role in many studies.[16–18] The Monte Carlo code MCML (Monte Carlo modeling of light transport in multilayered tissue) has been the gold standard for simulations of light transport in multilayer tissue,[15,19] but it is ineffective in the presence of 3D heterogeneity. In fact, the team has developed a software program targeted for Monte Carlo simulation of light propagation in voxelized media (MCVM).[16] Using the MCVM, we can better evaluate the relationship between photon propagation in VCH chest model and the layout between LSDs. At present, MCVM + VCH has been successfully used for studying the photon transmission distribution of brain, mammary gland, and heart, which showed the reliability of the MCVM+VCH method. However, this method has not been used for obtaining the photon migration characteristics of pulmonary artery yet.

In this study, thoracic tissues model of VCH dataset was adopted to improve the precision of chest structure modeling, and Monte Carlo simulation was carried out in combination with 3D voxelized media to establish a quantified and visualized photon migration human chest model. The SSD, the partial path-length factor (PPF),[15] the differential path-length factor (DPF),[16] and pulmonary artery signal contribution ratios of a series of separation of the LSD were calculated. The results showed that the degree of PE had a strong linear relationship with the detected signal

intensity. We simulate and visualize photon migration in human thoracic tissues with MCVM + VCH and the potential of noninvasive PE detection was first studied.

2 Materials and Methods

2.1 *Thoracic Model Built from the VCH*

The simulation was operated on a thoracic model established from the VCH dataset, which was a set of color photographs from the whole-body frozen sections. The VCH dataset was collected from a standing frozen Chinese male body (a donated cadaver) with little pathological alternations. In this study, we used 80 slices of photographic images of the VCH sections to complete the thoracic tissues region of the pulmonary artery from top to bottom, a photographic thoracic model of $436 \times 420 \times 80$ voxels was first built (Fig. 1). One voxel was defined as a $0.4 \times 0.4 \times 0.4$ mm^3 cubic. The whole model was divided into eight parts according to tissues that included skin, muscle, bone, subcutaneous fat, lung, Pa vessel wall, arteries, and venous blood. Please note that the voxels outside the thoracic tissues were assigned as air and did not participate in Monte Carlo simulation.

2.2 *Monte Carlo Simulation*

Monte Carlo simulation was used to deduce light propagation in the VCH of thoracic tissue. The Monte Carlo software used here was targeted for 3D voxelized media, the algorithm of which has been described in previous literature.[20] In theory, when a photon packet (or a single

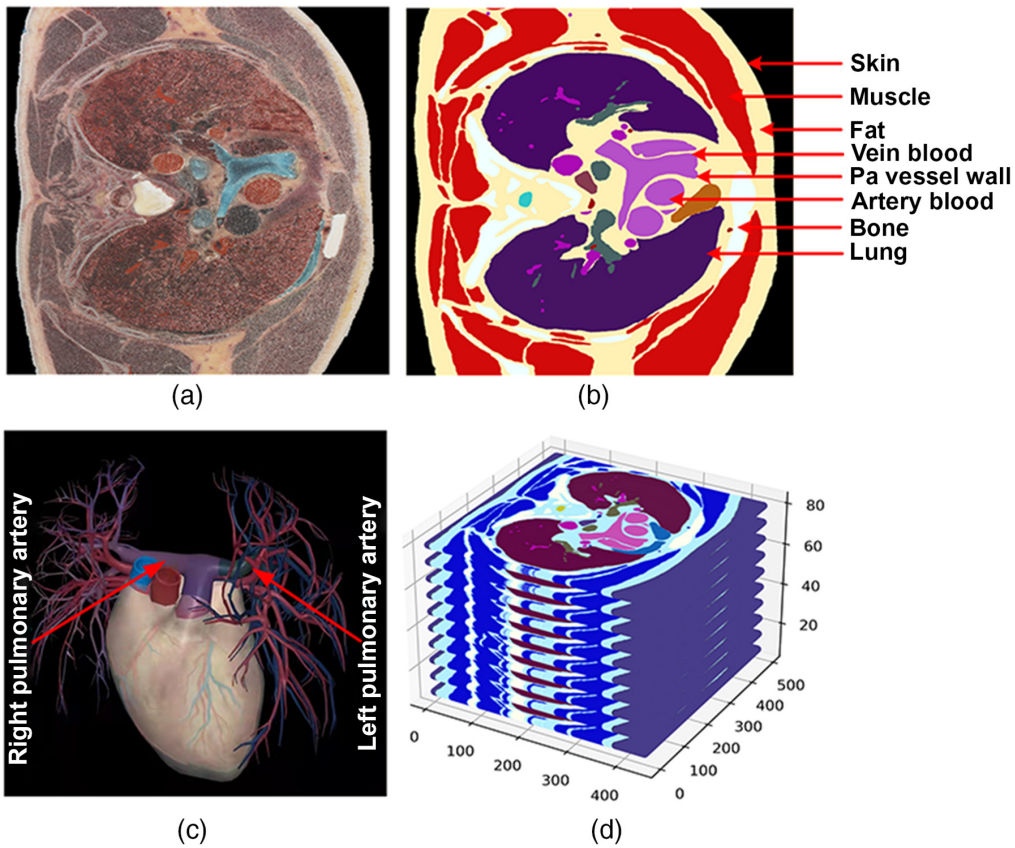

Fig. 1 The description of VCH thoracic models. (a) A representative original thoracic photography image from VCH. (b) The thoracic model was divided into eight tissue parts. (c) A representative graph of the pulmonary artery structure (an open access picture from 3D Human Body app). (d) The thoracic model was built to the 3D matrix of $436 \times 420 \times 80$ voxels.

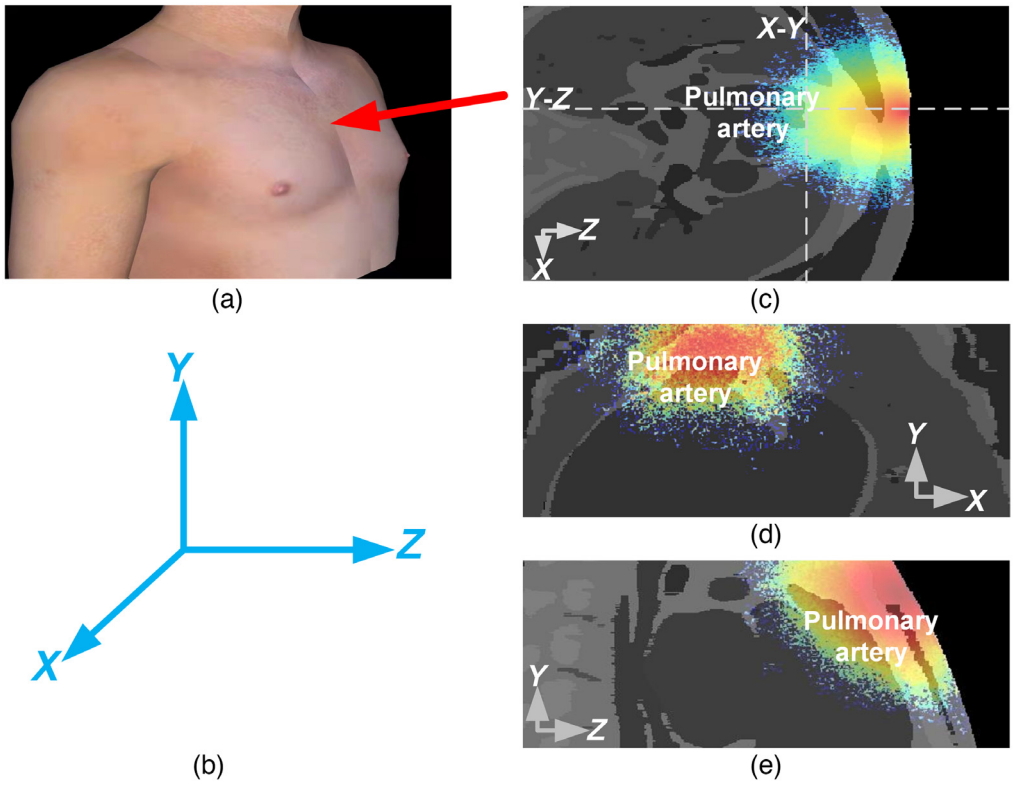

Fig. 2 Light fluence distribution in thoracic tissue under *X*-*Y*-*Z* field of view. (a) The position of the LSD on the human thoracic model. (b) The three-dimensional space coordinate system used in this study. (c) Light fluence in the *X*-*Z* plane scale is 436 × 420. (d) Light fluence in the *X*-*Y* plane scale is 436 × 80. (e) Light fluence in the *Y*-*Z* plane scale is 420 × 80.

photon) entered a tissue, it would be randomly scattered or continuously absorbed by the tissue media until it died.[21] Survival photons collected by the detector could be analyzed to get the valued information, such as intensity and propagation path length. In this study, a light source was placed upon in between the second and third anterior ribs, the detector was attached to the skin on the horizontal left side of the light source, and the axis directions were shown in the Fig. 2. The input light was the 800-nm IR light and other set up parameters were the same with the previous studies and shown in the Table 1.[30–32] Each simulation ejected 10^6 photons. After

Table 1 Optical properties of thoracic tissue at 800 nm.

Tissue type	n	μ_a (cm^{-1})	μ_s (cm^{-1})	g	References
Fat	1.33	0.083	134	0.910	22
Skin	1.37	0.20	73.7	0.715	23 and 24
Lung	1.40	1.0	95.0	0.910	25
Bone	1.43	0.11	291	0.936	26
Muscle	1.40	0.54	66.7	0.930	25
Pa vessel wall	1.40	0.92	103	0.930	27
Arterial blood	1.40	2.33	522	0.990	28 and 29
Venous blood	1.40	2.38	440	0.990	28 and 29

Where n is the refractive index of the medium, μ_a is the absorption coefficient, μ_s is the scattering coefficient, and g is the anisotropy factor.

Table 2 The parameters of S_A and S_V for the four groups.

Group	SaO_2 (%)	SvO_2 (%)
Level I	93	71
Level II	91	67
Level III	89	63
Normal	95	75

SaO_2 was the arterial blood oxygen saturation.
SvO_2 was the venous blood oxygen saturation.

10 times simulation, the average photon fluence was calculated for representing the light propagation results. Besides, two files were generated for respectively recording the absorbed photon numbers and output photon distribution. According to these two files, a series of photon transmission characters were calculated.

Three disease levels were designed for simulating the optical transmission on the patients. We change the relationship between arterial blood and venous blood μ_a parameter to change the blood oxygen saturation.[33] According to the variation of the arterial oxygen blood saturation (SaO_2) and the venous blood oxygen saturation (SvO_2), four groups were used in this study, including the three patient groups with mild (Level I), medium (Level II), and serious (Level III) disease, and the control group of normal people.[34] The parameter details were shown in the Table 2.

2.3 *Spatial Sensitivity Distribution*

One output file of MCVM program contained the photon absorption in every voxel of the whole tissue model. The spatial distribution of light absorption ($A(\vec{r}_s, \vec{r}_m)$),[35] a 3D matrix of $436 \times 420 \times 80$ voxels, can be obtained from this file. Equation (1) was used to calculate the weight of the light fluence ($F(\vec{r}_s, \vec{r}_m)$) from the light source coordinate position ($\vec{r}_s$) to a random voxel (m) position ($\vec{r}_m$).[35] The $\mu_a(\vec{r}_m)$ was the absorption coefficient of the tissue type at the m'th voxel.[35]

Then ($\mathrm{SSD}(\vec{r}_S, \vec{r}_D, \vec{r}_m)$) of the individual voxel was calculated by the three-point Green's Eq. (2).[36] $F(\vec{r}_D, \vec{r}_m)$ indicated the light fluence of a voxel ($\vec{r}_m$) at the ($\vec{r}_D$) location.[36] After collecting all the SSD value of voxels, the SSD of the whole model was calculated by summing all these voxel SSD value.[36] At the same time, the SSD of a specific tissue was calculated by summing all the voxel SSD value of this tissue.[37] The ratio of the SSD of a specific tissue to total SSD represented the involvement of this tissue type in the light transportation[35–37]

$$F(\vec{r}_s, \vec{r}_m) = \frac{A(\vec{r}_s, \vec{r}_m)}{\mu_a(\vec{r}_m)}, \tag{1}$$

$$\mathrm{SSD}(\vec{r}_S, \vec{r}_D, \vec{r}_m) = F(\vec{r}_S, \vec{r}_m) \times F(\vec{r}_D, \vec{r}_m). \tag{2}$$

2.4 *Separation of the LSD*

The most optimal separation of LSD was calculated. As mentioned above, the light source was placed between the second and third anterior ribs, where had few muscles and could penetrate more photons. The detector was placed horizontally to the left of the light source. The separation of the LSD was determined by two factors, such as DPF and PPF.

DPF was the scaling factor that relates source-detector separations to the average path length that light travels. The notion of a DPF implies the assumption that the chromophore change was global to the sampling region.[38] In contrast, PPF refers to a similar scaling factor but one that assumes a focal change. A PPF therefore represents a proportionality factor converting the

source-detector separation into the average path length that light travels through a focal region of chromophore change.[39,40]

The PPF of the pulmonary artery (PPFpa) was calculated from the file that recorded the output photon distribution. It represented the sensitivity of the detected light intensity signal to the pulmonary artery.[26] The PPFpa/DPF represented the contribution of pulmonary arterial tissue to the absolute absorption of photons. The optimal separation distance between the LSDs was reflected by such indicators of PPF and PPFpa/DPF.

3 Results

3.1 *Light Fluence Distribution*

As mentioned in the method part, light fluence distribution were drawn for indicating the photon existence in the thoracic tissues (Fig. 2). Penetrated photons could be observed reach to the pulmonary artery from any of the three views, such as *X*-*Z*, *X*-*Y*, and *Y*-*Z*. From the *X*-*Z* view, it was proved that the 800-nm light actually traveled through the sternum into the ribcage [Fig. 2(c)]. From the *Y*-*Z* light fluence distribution, it could be observed that photons scattered at the main pulmonary artery [Fig. 2(e)]. The *X*-*Y* distribution located at 33 mm toward the skin surface proved that photons could penetrate tissues to reach the pulmonary artery [Fig. 2(d)].

A representative light fluence distribution on the 40th slice of *X*-*Z* view was shown in the [Fig. 3(a)]. It showed that the light intensity was set up to have photons traveling at least 37 mm in the body. The light influence intensity in log10 scale decreased as photons traveled through the tissues from skin, fat, muscle, fat, and pulmonary artery to venous blood [Fig. 3(b)]. Similarly, the light influence intensity decreased sharply in the normal scale.[41] By a 3D coordinate system, set a center point position on the body surface (161, 333, and 40) and keep the *X*-axis and *Y*-axis unchanged. The photon attenuates from the incident point $Z = 333$ until the light intensity is close to 0. The distance from the incident point to the end point is the penetration depth.[17,42]

When the depth increased to the pulmonary artery surface, the intensity was 45/voxel. At the depth of 36 mm, the intensity decreased to 1/voxel, at which venous blood was. These data suggest that 800-nm photon could transport into the pulmonary artery at depth of 36 mm with a light source placed upon anterior sternum. Furthermore, the light intensity decreased about 2.2×10^4 times when the photons reached the pulmonary artery vessel wall.

3.2 *Effect of Source–Detector Separation*

L_{SD} affected spatial sensitivity profiles.[43] In this study, different L_{SD} was used for simulating the light propagation in the VCH thoracic lungs. The Fig. 4 showed the SSD on the 40th slice at various L_{SD}. The results showed that the penetration depth and detection area of the spatial

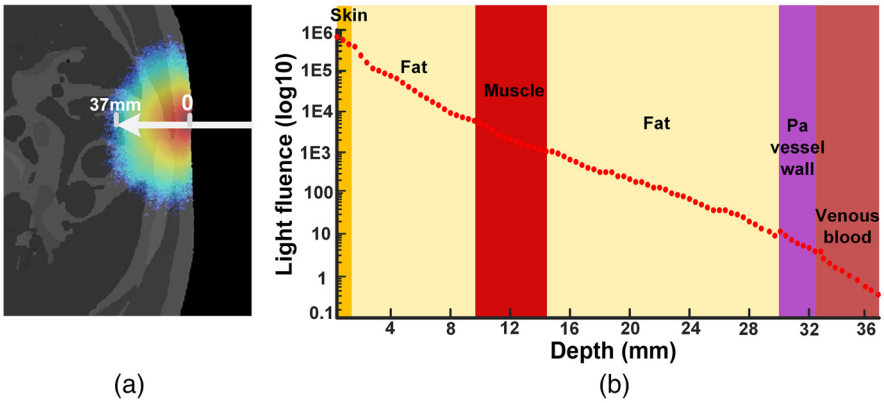

Fig. 3 The light influence intensity changed with tissue depth. (a) The light fluence distribution on the 40th slice. (b) The light fluence intensity decreased from skin to venous blood.

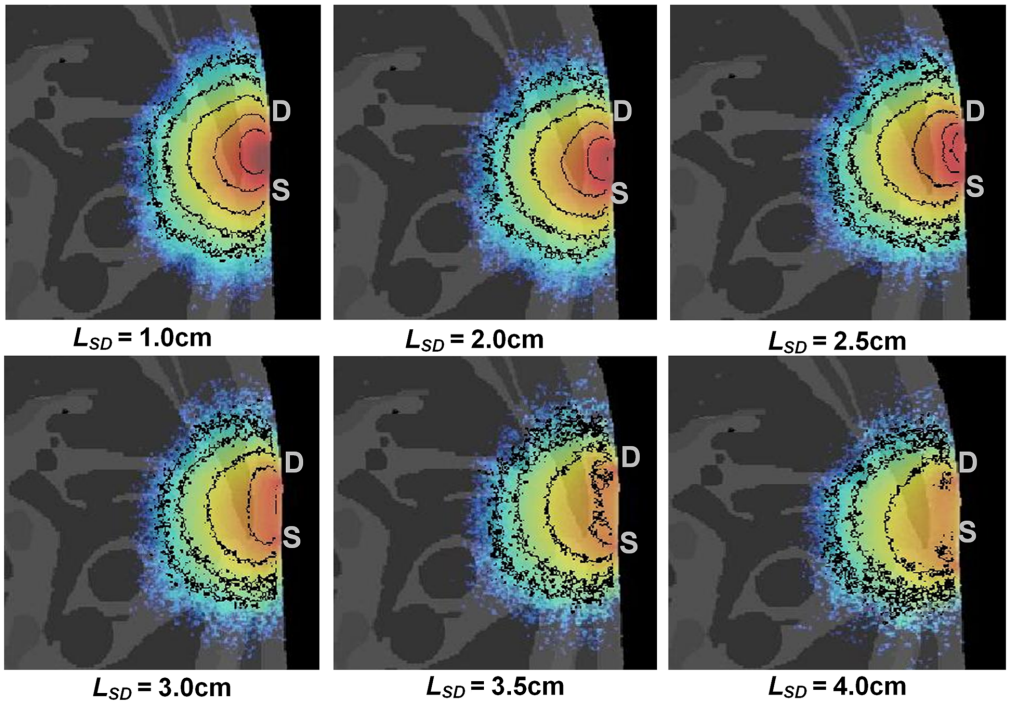

Fig. 4 Spatial sensitivity profiles varied with L_{SD}.

sensitivity profile gradually increased when the L_{SD} increased from 1.0 to 3.0 cm. When the L_{SD} increased from 3.0 to 4.0 cm, the detection area of the spatial sensitivity profile become broader but the penetration depth gradually decreased.

3.3 *Optimized Source–Detector Separation*

The optimal separation of the LSD was depended on PPFpa, PPFpa/DPF, and pulmonary artery photon absorption. As shown in Fig. 5(a), DPFs tended to increase exponentially with the incremental L_{SD}. Figure 5(b) showed that there was a different performance of PPFpa with L_{SD}. When the L_{SD} was in the range of 2.5 to 2.9 cm, the PPFpa increased rapidly. And then, the PPFpa dropped sharply. Figure 5(c) showed that the change of PPFpa/DPF was affected by L_{SD}. When the L_{SD} was in the range of 2.0 to 3.1 cm, the ratio of PPFpa/DPF increased gradually and then decreased sharply. There was a peak in between the 2.0 and 3.1 cm of L_{SD}. By comparing the Figs. 5(b) and 5(c), both the PPFpa and PPFpa/DPF gradually increased to the maximum value when the L_{SD} increased from 2.0 to 2.8 cm and then sharply dropped when the L_{SD} increased from 2.8 to 3.1 cm. Figure 5(d) showed the absorption of photons by main pulmonary artery at different L_{SD}. The absorption of photons rose slowly at initial and then decreased when the L_{SD} increased from 1 cm. The most optimal L_{SD} was about 2.8 to 3.1 cm where the photon adsorption reached the maximum of 4.6%. These results suggested that the optimized source-detector separation was in between the 2.8 to 3.1 cm.

3.4 *Pulmonary Embolism Impact on SSD*

The SSD also reflected the grade of PE.[44] Table 3 showed the SSD proportion of each tissue at different PE levels. In the pulmonary artery, the SSD proportions were 0.0131%, 0.0129%, 0.0127%, and 0.0126%, respectively, for the healthy people, Level I patient, Level II patient, and Level III patient. When the PE becomes serious, the SSD proportion decreased. The SSD proportions of arterial and venous blood, as well as lung at different PE degrees were also estimated. It showed that the SSD proportion in lung and venous blood slowly decreased when the PE level increased. However, the SSD proportions in arterial blood were almost zero. These

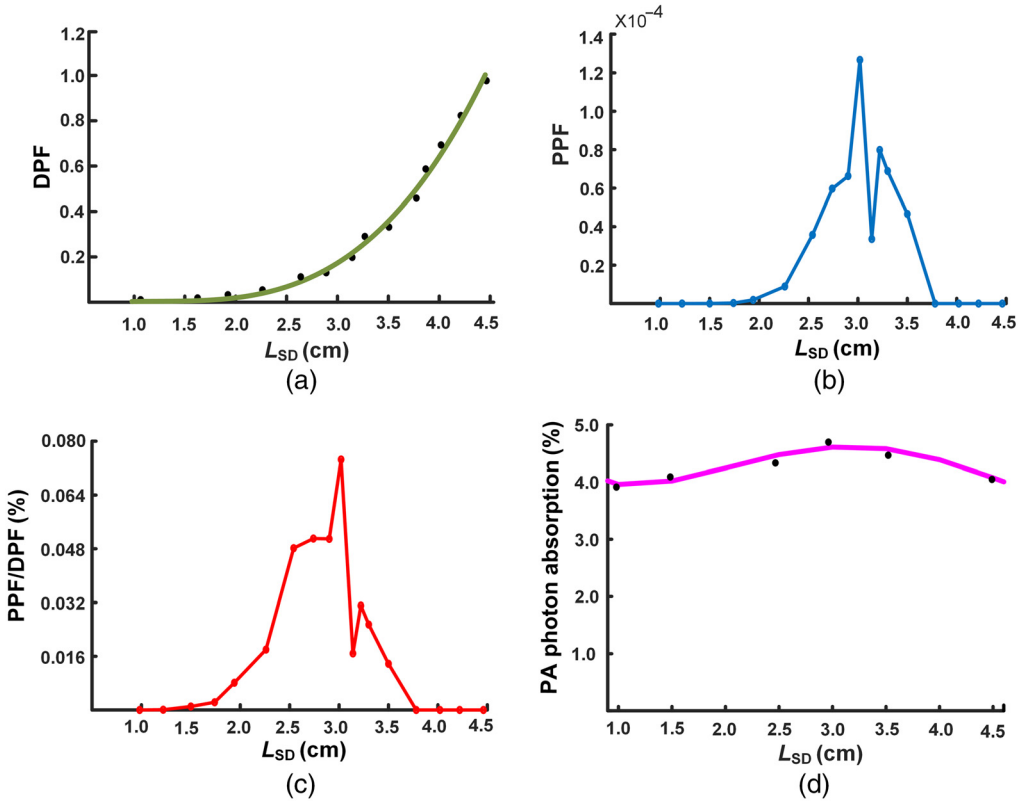

Fig. 5 The value of DPF, PPFpa, PPFpa/DPF, and photon absorption at various L_{SD}. (a) The DPF exponential growth. (b) The change of PPFpa at different L_{SD}. (c) The change of PPFpa/DPF at different L_{SD}. (d) The proportion of photon absorption at pulmonary artery.

Table 3 The proportion of SSD (%) of each tissue at different levels of PE.

Tissue type	Fat	Skin	Lung	Bone	Muscle	Pa vessel wall	Arterial blood	Venous blood
Normal	67.398	11.34	0.002	15.92	5.34	0.0131	0	0.004
Level I	67.638	11.21	0.002	15.84	5.31	0.0129	0	0.004
Level II	67.588	11.27	0.002	15.89	5.25	0.0127	0	0.003
Level III	67.867	11.19	0.001	15.65	5.28	0.0126	0	0.002

results indicated that the venous blood and lungs could be possibly used for detecting the PE by the SSD.

3.5 *Pulmonary Embolism Impact on Detected Light Intensity*

In the result of previous part, the optimal source–detector separation was around 2.9 cm. Hence, the L_{SD} was set to 2.9 cm for detecting the light intensity. In the result, light intensities were normalized to find the regular pattern (Fig. 6). Results showed that the normalized light intensity decreased as the PE level increased. Therefore, the light adsorption increased as the PE level increased. Though more photons were absorbed by the higher levels of PE, escaped photons were still detected by the detector. It proved that this detection method could be used for detecting the PE. The linear fitting function of normalized light intensity was ($r^2 = 0.998$, $p < 10^{-5}$). This linear relationship suggested that the PE level could be accurately estimated by the detected light intensity.[45]

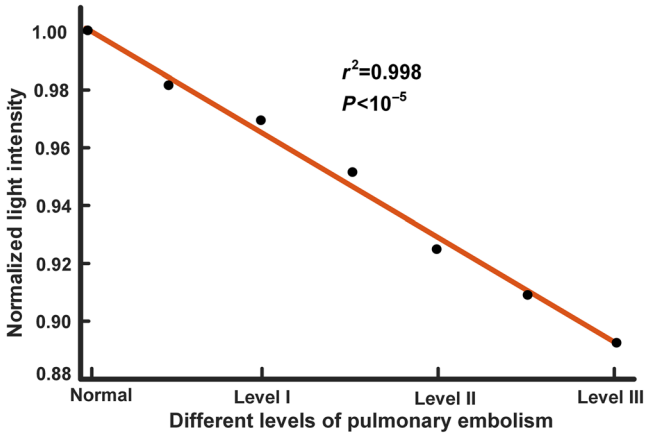

Fig. 6 Linear fitting of normalized light intensity as the level of PE increased.

4 Discussion and Conclusion

In this paper, the Monte Carlo simulation based on the VCH was used for simulating the light migration in human thoracic tissues. Importantly, the number of absorbed photons and light fluence distribution in thoracic tissues were indicated partial photons could reach to the pulmonary artery. Besides, the different levels of PE impact on photon detection were confirmed by venous blood SSD and output photon intensity. In addition, the detected light intensity was linearly related to the PE level. These results suggested that PE could be accurately diagnosed by NIRS. In the end, the optimized L_{SD}, 2.8 to 3.1 cm, was calculated by PPF, DPF, and the proportion of absorbed photons.

The optical parameters selected in this paper were obtained by the previous work of our group.[16,36,46] These parameters were from studies of various groups,[22–24,27] which were evaluated and confirmed by previous studies.[35,47] In this study, the simulation experiment was carried out in an ideal condition, that was, the influence of the connection between organizations was ignored. Parameters that measured directly from the real human body were not suitable for this study. In the future work, more reality conditions will be included in simulation conditions. Then, the selected parameters will be changed. In Pifferi's study, optical parameters of lung tissue were measured from the real human body, which included the influence of other tissue reaction.[10,11] These parameters will be selected in the future work.

The NIR light has better performance in penetration depth.[48] The pulmonary artery tissues get more light because of the low absorption coefficient of other tissues in NIRS, as presented in Table 1. In addition, the light source was placed on the skin upon the anterior sternum in this simulation. In the anterior sternum region, there were fewer muscles, and the distance between the skin and the pulmonary artery was relatively small, so the depth of the photon radiation into the pulmonary artery was greater. The photon distribution in the pulmonary artery tissues has been clearly displayed in Fig. 2. Moreover, the results suggest that certain photons may migrate to the surface of the body with optical information of the pulmonary artery tissues. After the incident light enters the human body, photons were absorbed and scattered in different tissues, and partial photons penetrate through the human skin, fat and bone then into the pulmonary artery.

The detector we use is a very common OPT101 (OPT101 Monolithic Photodiode and Single-Supply Transimpedance Amplifier).[49] The sensitivity of this detector expressed by noise effective power is about 1.86 $(\mathrm{mA/w})/\mathrm{cm}^2$ (800 nm), the size of photodiode is 2.29 mm $*$ 2.29 mm, and the size of OPT101 is 9.52 mm $*$ 6.52 mm. The OPT101 minimum detectable SSD signal is of order 10^{-6} to 10^{-7}, so our measured SSD signal of 0.002% is still theoretically within the measurable range of existing devices. During simulation, we can set the receiving area of the detector to make it as consistent as possible with the detection area of the detector in reality. As shown in Table 3, pulmonary artery proportion of SSD was about 0.0131% of the total SSD, Venous blood only accounts for 0.002%. These values indicate that the photodetector can capture those photons that carry optical information about the target tissue and can analyze the captured signal.

Our results identified the optimized separation of the LSD depending on the DPF and PPF in Fig. 5. The largest diameter in the thoracic model can be narrowed down to 2.8 to 3.1 cm. In previous study, the optimal source-detector separation was narrowed down to 3 to 3.5 cm in the head model.[50] PPFpa/DPF represents the contribution of the pulmonary artery to the absolute absorption measurement, and higher proportion value might be conducive to detection of absolute concentrations of oxyhemoglobin and deoxyhemoglobin to account for hemodynamics at the pulmonary artery. Actually, the separation distance between the light source and the detector was not as farther as better, when the distance was larger than 3.1 cm, the energy density of the emitted photon decreased rapidly, that seriously affected the detected signal quality.[51]

The PE was simulated in this study by produced different degrees of hypoxemia to simulate different levels of embolism at the pulmonary artery. The results showed that there were significant differences in optical performance of different PE levels in Fig. 6. The drop of light intensity reflected the embolism in the blood. The region beneath coverage of the NIRS probe contributes more sensitivity to NIRS measurements, and scattered photons outside this region can also be detected but with less reliability and sensitivity. This is a common problem with NIRS technology. Furthermore, as mentioned above, the light intensity variations could be a comprehensive outcome of various factors in the detected area, and light intensity as a single contrast agent sometimes may possibly issue a false alarm for embolism. The combination of multivariate modeling such as oxygen consumption and optical properties may make the prediction of PE more reliable. Nevertheless, to the best of our knowledge, this study was the first to study PE using an optical noninvasive approach.

From the simulation result, the light intensity could be an indicator of PE determination. In this study, the simulation experiment was carried out under ideal conditions, including the probe contacting the skin surface with zero distance and the probe not causing any pressure to the skin. The thickness and optical properties of the skin did not change. However, in human experiments, the light intensity is influenced by many factors, such as the optical contact distance between probe and tissue, optical properties and thickness of the skin, and the pressure of the probe to the tissue. Based on the simulation results, more real conditions will be considered in the future work of simulation and instrument design. Lightweight detectors might be used for constructing the instrument to reduce the pressure between the probe and the skin and reduce the influence to the detected light intensity. In addition, the tissue optical properties also change with the human exhalation and inhalation. In this study, the average value of the light intensity at exhalation and inhalation status was calculated to eliminate this change influence that represented a relative ideal condition. More complicated reality conditions of exhalation and inhalation will be considered in the future.

In conclusion, the present study employed the thoracic model of visible Chinese human and Monte Carlo simulation to investigate noninvasive detected of the PE levels. The study found that photons could reach the pulmonary artery tissue and the light intensity was linearly related to the degrees of embolism. The appearance of PE can produce lower intensity, which could be used as a reflection on the presence of embolus in pulmonary artery. Overall, this study demonstrated the great potential of NIRS in detecting PE.

Disclosures

The authors have no relevant financial interests in this article and no potential conflicts of interest to disclose.

Acknowledgments

This study was supported by the National Natural Science Foundation of China (Grant No. 81971660), Tianjin Outstanding Youth Fund Project (Grant No. 20JCJQIC00230), Sichuan Science and Technology Program (Grant No. 2021YFH0004), Medical & Health Innovation Project, Chinese Academy of Medical Sciences, & Peking Union Medical College (Grant Nos. 2021-I2M-1-058, 2021-I2M-1-042, 2022-I2M-C&T-A-005, and 2022-I2M-C&T-B-012).

References

1. J. Gribbin et al., "Incidence and mortality of idiopathic pulmonary fibrosis and sarcoidosis in the UK," *Thorax* **61**, 980–985 (2006).
2. K. A. Martin et al., "Time trends in pulmonary embolism mortality rates in the United States," *J. Am. Heart. Assoc.* **9**, e016784 (2020).
3. R. W. Yeh et al., "Population trends in the incidence and outcomes of acute myocardial infarction," *N. Eng. J. Med.* **362**, 2155–2165 (2010).
4. F. Klok, M. Delcroix, and H. J. Bogaard, "Chronic thromboembolic pulmonary hypertension from the perspective of patients with pulmonary embolism," *J. Thromb. Haemostasis* **16**, 1040–1051 (2018).
5. T. Li et al., "Simultaneous measurement of deep tissue blood flow and oxygenation using noncontact diffuse correlation spectroscopy flow-oximeter," *Sci. Rep.* **3**, 1385 (2013).
6. T. Li et al., "Bedside monitoring of patients with shock using a portable spatially-resolved near-infrared spectroscopy," *Biomed. Opt. Express.* **6**, 3431–3436 (2015).
7. T. Li, Q. Luo, and H. Gong, "Gender-specific hemodynamics in prefrontal cortex during visual verbal working memory by near-infrared spectroscopy," *Behav. Brain Res.* **209**(1), 148–153 (2010).
8. B. Pan et al., "Noninvasive and sensitive optical assessment of brain death," *J. Biophotonics* **12**, e201800240 (2019).
9. K. B. Gan, E. Zahedi, and M. A. Ali, "Transabdominal fetal heart rate detection using NIR photoplethysmography: instrumentation and clinical results," *Trans. Biomed. Eng.* **56**(8), 2075–2082 (2009).
10. G. Quarto et al., "Time-resolved optical spectroscopy of the chest: is it possible to probe the lung?" in *Eur. Conf. Biomed. Opt.*, Optical Society of America (2013).
11. A. Pifferi et al., "Initial non-invasive in vivo sensing of the lung using time domain diffuse optics," arXiv preprint arXiv:2205.08211 (2022).
12. A. W. Dunn et al., "In-vitro depth-dependent hyperthermia of human mammary gland adenocarcinoma," *Mater. Sci. Eng.* **69**, 12–16 (2016).
13. T. Li et al., "Noninvasive diagnosis and therapeutic effect evaluation of deep vein thrombosis in clinics by near-infrared spectroscopy," *J. Biomed. Opt.* **20**(1), 010502 (2015).
14. S. Yavuz et al., "Surgical embolectomy for acute massive pulmonary embolism," *Int. J. Clin. Exp. Med.* **7**, 5362–5375 (2014).
15. T. Li, H. Gong, and Q. Luo, "Visualization of light propagation in visible Chinese human head for functional near-infrared spectroscopy," *J. Biomed. Opt.* **16**(4), 045001 (2011).
16. T. Li, H. Gong, and Q. Luo, "MCVM: Monte Carlo modeling of photon migration in voxelized media," *J. Innov. Opt. Health Sci.* **3**, 91–102 (2010).
17. T. Li et al., "Photon penetration depth in human brain for light stimulation and treatment: A realistic Monte Carlo simulation study," *J. Innov. Opt. Health. Sci.* **10**, 1743002 (2017).
18. S. Zhang et al., "The Chinese Visible Human (VCH) datasets incorporate technical and imaging advances on earlier digital humans," *J. Anat.* **204**, 165–173 (2004).
19. L. Wang, S. L. Jacques, and L. Zheng, "MCML—Monte Carlo modeling of light transport in multi-layered tissues," *Comput. Methods Prog. Biomes.* **47**,131–146 (1995).
20. M. A. Kamran, M. Mannann, and M. Jeong, "Differential path-length factor's effect on the characterization of brain's hemodynamic response function: a functional near-infrared study," *Front. Neuroinform.* **12**, 37 (2018).
21. S. L. Jacques, *Monte Carlo Modeling of Light Transport in Tissue (Steady State and Time of Flight)*, Vol. **32**, pp. 109–144, Springer, Dordrecht (2010).
22. C. R. Simpson et al., "Near-infrared optical properties of ex vivo human skin and subcutaneous tissues measured using the Monte Carlo inversion technique," *Phys. Med.* **43**(9), 2465 (1998).
23. R. Marchesini et al., "Optical properties of in vitro epidermis and their possible relationship with optical properties of in vivo skin," *J. Photochem. Photobiol. B: Biol.* **16**(2), 127–140 (1992).
24. W. A. Bruls and J. C. Leun, "Forward scattering properties of human epidermal layers," *Photochem. Photobiol.* **40**(2), 231–242 (1984).

25. A. N. Bashkatov et al., "Optical properties of human skin, subcutaneous and mucous tissues in the wavelength range from 400 to 2000 nm," *J. Phys.* **38**(15), 2543 (2005).
26. A. M. Nilsson, R. Berg, and S. Andersson, "Integrating sphere measurements of tissue optical properties for accurate photodynamic therapy (PDT) dosimetry laser interaction with hard and soft tissue," *Proc. SPIE* **2323**, 47–57 (1995).
27. J. F. Beek et al., "In vitro double-integrating-sphere optical properties of tissues between 630 and 1064 nm," *Phys. Med.* **42**(11), 2255 (1997).
28. A. Roggan et al., "Optical properties of circulating human blood in the wavelength range 400 to 2500 nm," *J. Biomed. Opt.* **4**(1), 36–46 (1999).
29. M. Friebel et al., "Determination of optical properties of human blood in the spectral range 250 to 1100 nm using Monte Carlo simulations with hematocrit-dependent effective scattering phase functions," *J. Biomed. Opt.* **11**(3), 034021 (2006).
30. Y. Liu et al., "Monte Carlo and phantom study in the brain edema models," *J. Innov. Opt. Health. Sci.* **10**, 1650050 (2017).
31. I. Nishidate et al., "In vivo estimation of light scattering and absorption properties of rat brain using a single-reflectance fiber probe during cortical spreading depression," *J. Biomed. Opt.* **20**(2), 027003 (2015).
32. S. L. Jacques, "Optical properties of biological tissues: a review," *Phys. Med. Biol.* **58**, R37–R61 (2013).
33. C. Du et al., "Quantification of NIRS data of a blood phantom by spectral multicomponent analysis," *Proc. SPIE* **2626**, 130–140 (1995).
34. S. Erol et al., "Is oxygen saturation variable of simplified pulmonary embolism severity index reliable for identification of patients, suitable for outpatient treatment," *Clin. Respir. J.* **12**, 762–766 (2018).
35. L. Wu, Y. Lin, and T. Li, "Effect of human brain edema on light propagation: a Monte Carlo modeling based on the Visible Chinese Human Dataset," *IEEE. Photonics J.* **9**, 1–10 (2017).
36. W. Liu et al., "Monte Carlo modeling of photon migration in realistic human thoracic tissues for noninvasive monitoring of cardiac hemodynamics," *J. Biophotonics* **12**, e201900148 (2019).
37. D. A. Boas and A. M. Dale, "Simulation study of magnetic resonance imaging-guided cortically constrained diffuse optical tomography of human brain function," *Appl. Opt.* **44**, 1957–1968 (2005).
38. G. Strangman, M. A. Franceschini, and D. A. Boas, "Factors affecting the accuracy of near-infrared spectroscopy concentration calculations for focal changes in oxygenation parameters," *Neuroimage* **18**, 865–879 (2003).
39. Y. Fukui, Y. Ajichi, and E. Okada, "Monte Carlo prediction of near-infrared light propagation in realistic adult and neonatal head models," *Appl. Opt.* **42**, 2881–2887 (2003).
40. J. Steinbrink et al., "Determining changes in NIR absorption using a layered model of the human head," *Phys. Med. Biol.* **46**, 879–896 (2001).
41. D. R. Snelling et al., "A calibration-independent laser-induced incandescence technique for soot measurement by detecting absolute light intensity," *Appl. Opt.* **44**, 6773–6785 (2005).
42. F. Martelli et al., "There's plenty of light at the bottom: statistics of photon penetration depth in random media," *Sci. Rep.* **6**, 27057 (2016)
43. G. E. Strangman, Z. Li, and Q. Zhang, "Depth sensitivity and source-detector separations for near infrared spectroscopy based on the Colin27 brain template," *PLos One* **8**, e66319 (2013).
44. M. J. Page et al., "Non-invasive imaging and cellular tracking of pulmonary emboli by near-infrared fluorescence and positron-emission tomography," *Nat. Commun.* **6**, 8448 (2015).
45. W. Xiong et al., "The relationship between tumor markers and pulmonary embolism in lung cancer," *Oncotargt* **8**, 41412 (2017).
46. T. Li et al., "Optimize illumination parameter of low-level laser therapy for hemorrhagic stroke by Monte Carlo simulation on Visible Human dataset," *IEEE Photonics J*, **10**(3), 6100409 (2018).
47. X. Fang et al., "Effect of scalp hair follicles on NIRS quantification by Monte Carlo simulation and Visible Chinese Human Dataset," *IEEE Photonics J.* **10**(5), 1–10 (2018).

48. N. J. Cuper et al., "The use of near-infrared light for safe and effective visualization of subsurface blood vessels to facilitate blood withdrawal in children," *J. Biomed. Eng.* **35**, 433–440 (2013).
49. T. Li et al., "A brief review of OPT101 sensor application in near-infrared spectroscopy instrumentation for intensive care unit clinics," *Sensors* **17**(8), 1701 (2017).
50. W. L. M. Izzetoglu, "Investigation of the source-detector separation in near infrared spectroscopy for healthy and clinical applications," *J. Biophotonics* **12**, e201900175 (2019).
51. D. Li et al., "Near-infrared excitation emission and multiphoton-induced fluorescence of carbon dots," *Adv. Mater.* **30**, 1705913 (2018).

Biographies of the authors are not available.